Polyhierarchically structured TiP_2O_7/C microparticles with enhanced electrochemical performance for lithium-ion batteries

Yanru Sun[a], Ligang Gai[a]*, Yan Zhou[a], Xinzhu Zuo[b], Jianhua Zhou[a], and Haihui Jiang[a]

[a]*School of Chemistry and Pharmaceutical Engineering, Qilu University of Technology, Jinan 250353, People's Republic of China*

[b]*School of Material Science & Engineering, Qilu University of Technology, Jinan 250353, People's Republic of China*

*Correspondence to whom should be addressed: liganggai@qlu.edu.cn

Electronic Supplementary Information

Table of contents

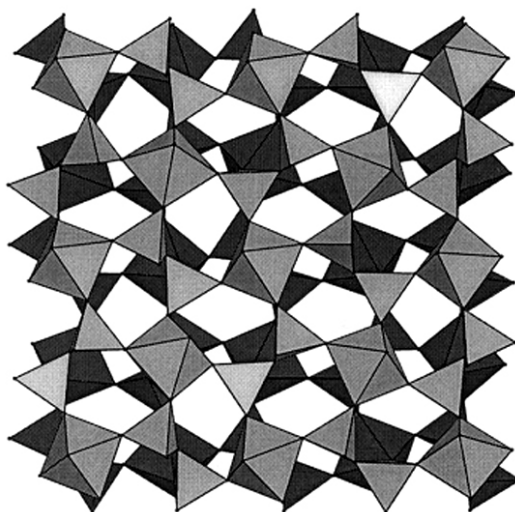## S1. Schematic illustration of TiP$_2$O$_7$ structure

Fig. S1. Schematic illustration of TiP$_2$O$_7$ structure[1]

S2. Theoretical calculations

The geometric structures of phytic acid (PA) molecule were optimized by using B3LYP method of density functional theory (DFT) at the 6-31G(d) basis sets. All the calculations were performed with the Gaussian 03 program package.
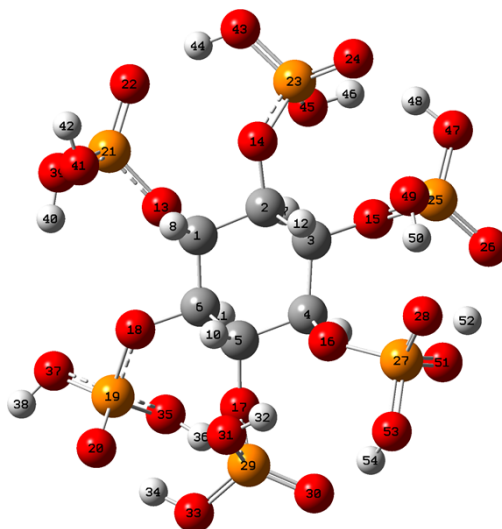

Fig. S2. The most stable molecular configuration of PA obtained by theoretical calculations at the 6-31G(d) basis sets: the dark grey, orange, red, and light grey spheres denote C, P, O, and H atoms, respectively.

Table S1. Parameters of the most stable molecular configuration of PA obtained by theoretical calculations at the 6-31G(d) basis sets.

Bond type	O20···H34	O22···H44	O24···H48	O26···H52	O28···H50	O30···H54	O37H40
Bond length (Å)	1.69144	1.69346	1.64271	1.60292	1.66864	1.69096	3.19020
Bond type	O20···O33	O22···O43	O24···O47	O26···O51	O28···O49	O30···O53	O37O39
Bond length (Å)	2.67417	2.68542	2.63787	2.59868	2.64625	2.65545	4.14962
Hydrogen bond	O20H34O33	O22 H44O43	O24H48O47	O26H52O51	O28H50O49	O30H54O53	
Bond angle (°)	166.32854	171.71903	171.46395	164.04325	162.16264	160.60236	

Dihedral angle set	P19P21P23P25	P19P21P23P27	P19P21P23P29	P19P21P25P27	P19P21P25P29
Dihedral angle (°)	−20.97747	−22.33488	−15.33678	−22.53792	−13.02273
Dihedral angle set	P19P21P27P29	P19P23P25P27	P19P23P25P29	P19P23P27P29	P19P25P27P29
Dihedral angle (°)	−10.55094	−16.26373	−6.88710	−3.25988	1.76499
Dihedral angle set	P21P23P25P27	P21P23P25P29	P21P23P27P29	P21P25P27P29	P23P25P27P29
Dihedral angle (°)	−3.07091	6.30573	13.23665	17.76348	19.28897
Dihedral angle set	P19P21P23C1	P19P21P23C2	P19P21P23C3	P19P21P23C4	P19P21P23C5
Dihedral angle (°)	−14.92206	−10.25075	−20.52210	−14.50888	−15.26697
Dihedral angle set	P19P21P23C6				
Dihedral angle (°)	−5.26742				

Fig. S2 shows the most stable molecular configuration of PA. The bond length of O···H and O···O, bond angle of ∠O–H···O, and dihedral angle of each set involving four phosphorous atoms are given in Table S1. As demonstrated in literature,[2,3] phosphates exhibit strong hydrogen bonds due to coexistence of strong acceptor and

donor centers. The strength or length of an O–H···O hydrogen bond is conveniently expressed by the distance between the donor and acceptor O atoms.[4] A distance larger than 2.7 Å is considered to be a weak hydrogen bond, a separation by 2.5–2.7 Å represents a strong hydrogen bond, and a distance below 2.5 Å defines a very strong hydrogen bond.[2] As shown in Table S1, the O···H and O···O bond length lie in the range of 1.6–1.7 Å and 2.59–2.69 Å, respectively, indicating that strong hydrogen bonding exists between the six $-H_2PO_4$ groups,[2,3] aside from the situation between the two $-H_2PO_4$ groups upon C1 and C6 (Fig. S2). The distance between O37 and O39, which separately belong to $-H_2PO_4$ groups upon C6 and C1, is 4.14962 Å, larger than 3.0 Å for the upper limit of O–H···O distance[5] and 3.22 Å for the sum of van der Waals radii,[6] indicating that there is no hydrogen bonding between the two $-H_2PO_4$ groups. In addition, the bond angle values of O–H···O present in Table S1 are all higher than 160°, also supporting strong hydrogen bonding exists as discussed above.[3,5] Significantly, the average dihedral angle absolute value of the six $-H_2PO_4$ groups is 11.96°. Moreover, the average dihedral angle absolute value between the $-H_2PO_4$ groups and the carbon ring is 13.46°. These results indicate that both the six $-H_2PO_4$ groups and the PA configuration are approximately located in one plane, probably due to the strong hydrogen bonding between adjacent $-H_2PO_4$ groups.

S3. Summary of the reported results on electrochemical performance of TiP_2O_7

Table S2. Summary of the electrochemical performance with respect to TiP_2O_7.

Sample	Initial discharge capacity (mAh g^{-1})/capacity retention (%)/cycle number at various rates										Refs. in ESI†
	0.1 C	0.12 C	0.167 C	0.2 C	0.5 C	1 C	1.67 C	2 C	5 C	10 C	
TiP_2O_7/C	125/100/10	–	–	126/100/10	136/99.3/100	127/95.1/100	–	116/93.2/200	95/94.4/400	59/98.4/100	this work
TiP_2O_7	99/97.4/10	–	–	129/98.9/10	123/98.3/100	113/99.7/50	–	77/82/20	25/80.7/10	–	this work
Mesoporous TiP_2O_7	98	–	–	–	–	57	–	–	–	–	11
TiP_2O_7 nanoplates	–	–	112.9/80.2/50	–	–	–	101.4/77/60	–	–	–	12
TiP_2O_7 nanoparticles	–	69±3/87/100	–	–	–	–	–	–	–	–	13
TiP_2O_7 microparticles	115.6/86.5/100	–	–	–	–	–	–	–	–	–	14
TiP_2O_7 microparticles	90	–	–	–	–	–	–	–	–	–	15
TiP_2O_7 submicroparticles	–	110/76.1/100	–	–	98/51.6/100	–	–	–	–	–	16

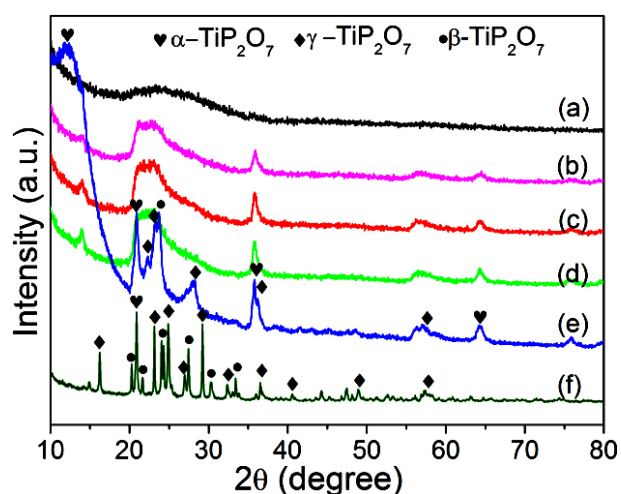**S4. XRD patterns of the titanium hydrogen phosphate hydrate (THPH)**

Fig. S3. XRD patterns of the THPH samples prepared with PA at 190 °C for: (a) 3 h; (b) 6 h; (c) 7.5 h; (d) 9 h; (e) 12 h; and (f) 6 h with H_3PO_4 instead of PA.

Fig. S3a–e shows the XRD patterns of the precursor samples prepared with PA at 190 °C, as a function of the reaction time. The XRD pattern of the sample prepared with H_3PO_4 at 190 °C for 6 h is also given for comparison (Fig. S3f). Apart from the amorphous sample obtained at 3 h (Fig. S3a), the degree of crystallinity of the samples prepared with PA is gradually improved as the reaction time increases. As shown in Figs. S3e and f, the samples are composed of α-, β-, and γ-phases of THPH, referred to JCPDS 44-0382, 46-0299, and 44-0383, respectively. It should be pointed out that the THPH sample prepared with PA (Fig. S3e) mainly consist of α- and γ-phases in low degree of crystallinity, whereas the well-crystallized THPH sample prepared with H_3PO_4 (Fig. S3f) has more diffraction peaks assigned to β-THPH. This result indicates that PA retards the growth of THPH grains due to step by step release of phosphate groups from PA,[7] leaving remnant *myo*-inositol and inositol phosphates

(IPs) staying in or upon the growing grains, resulting in the decrease in degree of crystallinity.

By examining the cell parameter c of α-THPH, it is found that the cell parameter c for the sample prepared with PA (Fig. S3b) is 15.3468 Å, larger than that of 15.0978 Å for the sample prepared with H_3PO_4 (Fig. S3f) under otherwise identical reaction conditions. The decrease in cell parameter c is attributed to the reduction of interactions between the layers stacked along the c-axis,[8] probably due to the existence of *myo*-inositol molecules in the interlayer of THPH.
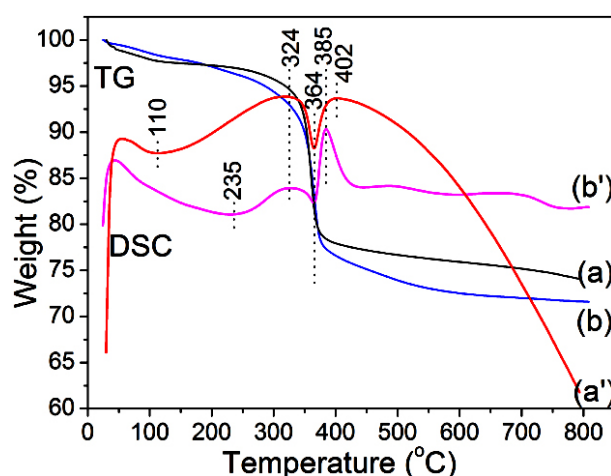
S5. TG/DSC analysis

Fig. S4. TG/DSC curves of THPH prepared with PA at 190 °C for 12 h: (a and a') annealed in N_2; (b and b') annealed in air.

The thermal behavior of THPH prepared with PA (190 °C, 12 h) was investigated by TG/DSC, as shown in Fig. S4. The weight loss at temperatures lower than ~250 °C is assigned to the elimination of surface-adsorbed water and ethanol, corresponding to endothermal peaks around 110 °C and 235 °C for the sample annealed in N_2 (curve a') and air (curve b'), respectively. The sharp weight loss appearing at temperatures

ranging from 235 to 380 °C is due to decomposition of *myo*-inositol/IPs and dehydration of hydrate water residing in interlayer of THPH. The decomposition of surface-adsorbed *myo*-inositol/IPs corresponds to the broad exothermal peaks centered at 324 °C, and the dehydration of hydrate water corresponds to the sharp endothermal peaks at 364 °C. A noteworthy point is that the TG curves for THPH separately annealed in N_2 and air insect at 188 °C and 356 °C to form a temperature hysteresis loop. This result is attributed to the different thermal behaviors of *myo*-inositol and IPs annealed in air and N_2; namely, the former is in the form of combustion without leaving carbon, and the latter produces carbon as a result of thermal decomposition. Although the remnant carbon does not change the dehydration temperature of THPH to form anhydrous titanium hydrogen phosphate (THP), further phase transformation from THP to TiP_2O_7 is retarded by the carbon for THPH annealed in N_2. This is evidenced by a broad exothermal peak at 402 °C in curve a' and a sharp exothermal peak at 385 °C in curve b'.

The weight percent of the remnant carbon can be calculated to be 2.48% from the data of TG curves, by subtracting the weight retention of 71.59% in curve b from that of 74.07% in curve a. The weight loss from the hydrate water in THPH can be calculated to be ~9.12% through the data at 324 °C and 364 °C in curve b, presenting a chemical formula of $Ti(HPO_4)_2 \cdot 1.24H_2O$ for THPH obtained at 12 h.

S6. FT-IR spectra of THPH and *myo*-inositol

Fig. S5a shows the IR spectrum of THPH prepared with PA. The IR spectrum of *myo*-inositol with analytical grade is provided for comparison (Fig. S5b). In Fig. S5a, the peaks centered at 2923, 1396, 1123, and 668 cm^{-1} correspond separately to v(C–H), δ(C–H), v(C–OP), and γ(C–H) vibrations of inositol, overlapping in peak position with those in Fig. S7b. This result confirms the adsorption of inositol/IPs upon THPH. The inositol and IPs arise from release of phosphate groups from PA in a solvothermal environment.[7]
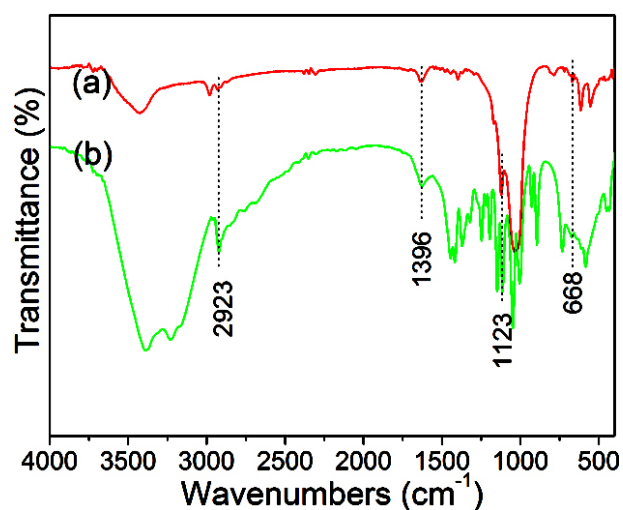

Fig. S5. FT-IR spectra of THPH prepared with PA at 190 °C for 12 h (a) and *myo*-inositol with analytical grade (b).
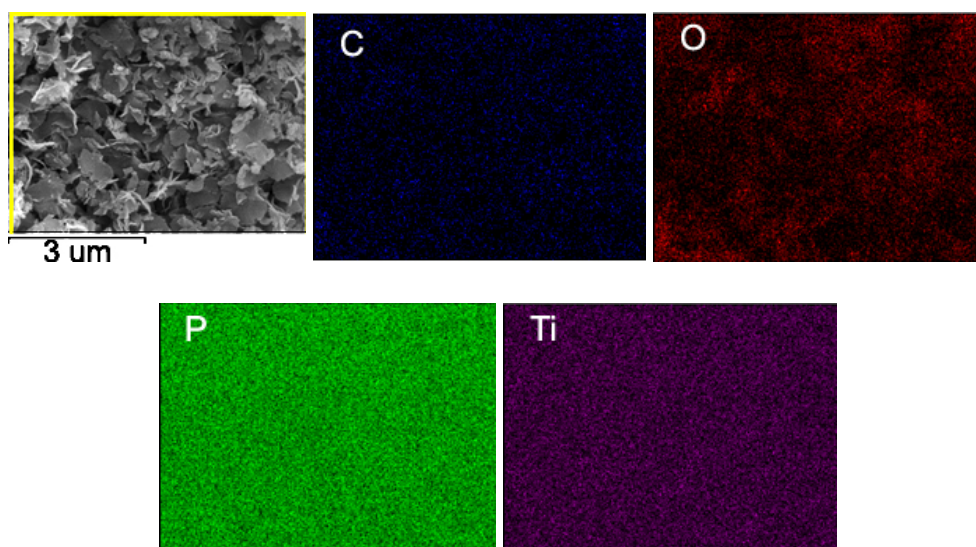
S7. SEM mapping images of TiP$_2$O$_7$/C and THPH

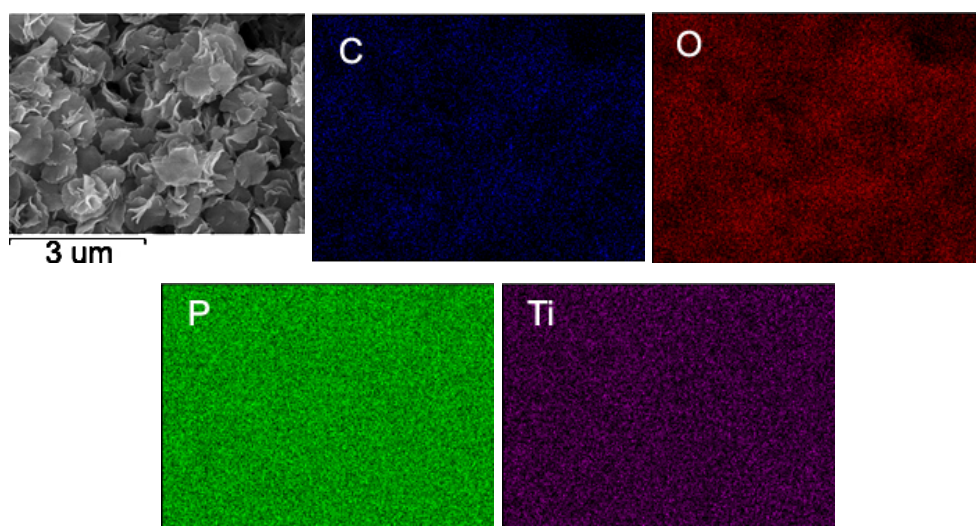**Fig. S6.** SEM mapping images of elemental C, O, P, Ti for TiP$_2$O$_7$/C.

Fig. S7. SEM mapping images of elemental C, O, P, Ti for THPH.

S8. SEM images of THPH prepared with H$_3$PO$_4$

Fig. S8 shows the SEM images of the THPH samples prepared with H$_3$PO$_4$ (85%) at

190 °C for 6, 7.5, and 12 h, respectively. It is apparent that the samples prepared with

H$_3$PO$_4$ are much different from those prepared with PA (Fig. 4 in the text). The

samples prepared with 6 h and 7.5 h (Fig. S8a and b) are mainly composed of

nanoplates. The size range of nanoplates in Fig. S6b (100–240 nm) is similar to that in

Fig. S8a (100–260 nm), whereas the thickness of nanoplates in Fig. S8b (30–60 nm) is less than that in Fig. S8a (50–90 nm). The decrease in thickness with increasing the reaction time is probably due to exfoliation of THPH with layered structure in a solvothermal environment.[8] As the reaction time increases to 12 h, the resulting product turns out to be aggregated nanoparticles with size in the range of 90–250 nm, much different from the flower-like microparticles prepared with PA.
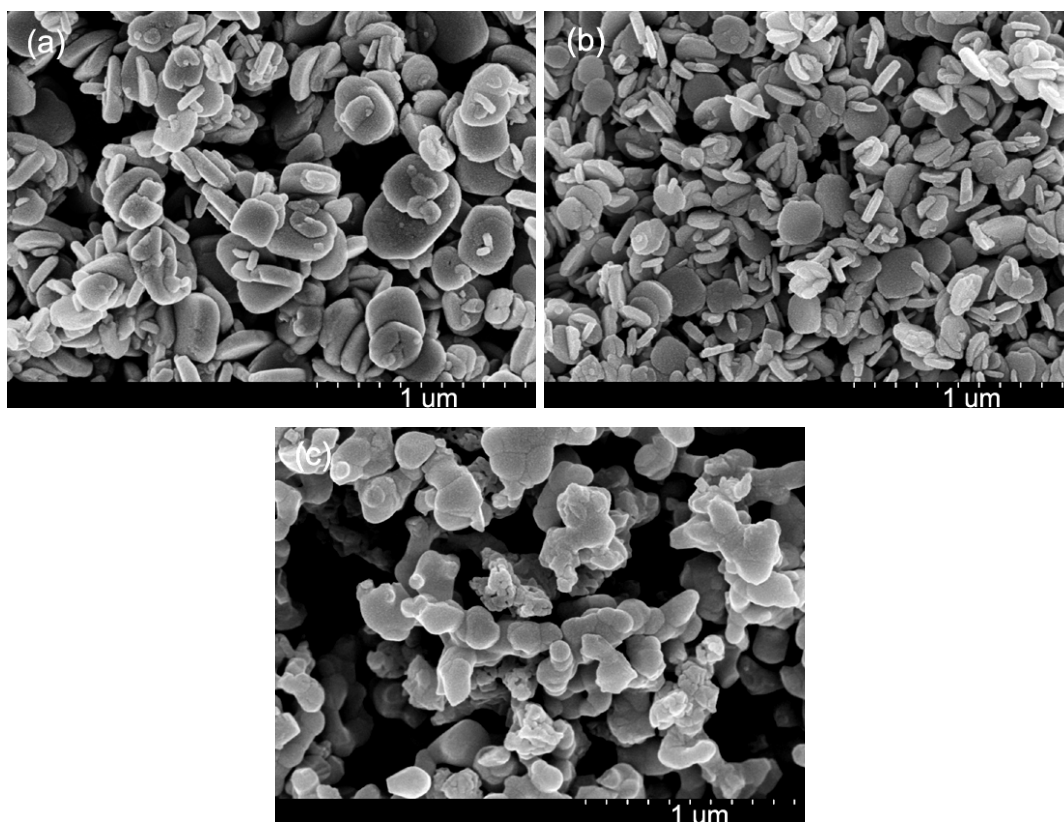

Fig. S8. SEM images of THPH prepared with H_3PO_4 (85%) at 190 °C for: (a) 6 h; (b) 7.5 h; (c) 12 h.

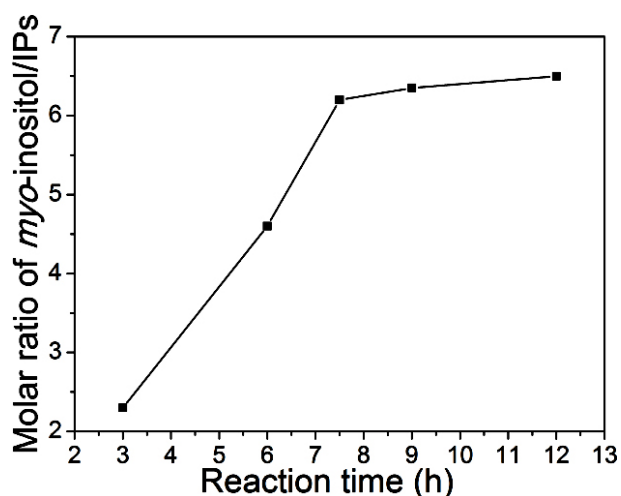## S9. High performance liquid chromatography (HPLC) analysis

Fig. S9. Variation plot of molar ratio of *myo*-inositol/IPs versus reaction time.

The variation in molar ratio of *myo*-inositol/inositol phosphates in reaction medium was examined as a function of reaction time on a Shimadzu SPD-10A HPLC equipment, using a Diamonsil C_{18} column (5 μ, 150 × 4.6 mm) for separation and 10% (v/v) methanol aqueous solution as the eluting solvent. The water used for HPLC was purified by double distillation. The solvent elution rate was 1 mL min^{-1}. The inositol phosphates (IPs) include mono-, di-, tris-, tetrakis-, and pentakis-phosphates, i.e. IP1, IP2, IP3, IP4, and IP5, respectively.[7] We do not attempt to differentiate the contributions from individual inositol phosphate in the calculations due to lack of their reference standards.

Fig. S9 shows the variation plot of molar ratio of *myo*-inositol/IPs versus reaction time. It is found that the molar ratio of *myo*-inositol/IPs increases as the reaction time increases, and stabilizes with reaction time more than 7.5 h, a time agrees well with that at which nanoflakes emerge in multitude. This result provides indirect evidence to support our suggestion that phosphate groups detach from the six-member carbon ring

and combine with titanate to form titanium hydrogen phosphate hydrate (THPH) within the reaction time of 3–6 h, leaving some *myo*-inositol staying in interlayers of the THPH structure. Before 3 h, dihydrogen phosphate groups interact with titanium ions due to strong coordination belonging to the phosphate groups,[9,10] and still remain on the six-member carbon framework in view of the low molar ratio of *myo*-inositol/IPs and the amorphous product obtained at 3 h (Fig. S3a). The *myo*-inositol molecules inside the interlayers reduce interactions between the layers stacked along the *c*-axis. After 6 h, the layers of THPH precursor tend to exfoliate to form THPH nanoflakes at 7.5 h, accompanying with *myo*-inositol in interlayers being released into the reaction medium. With prolonging the reaction time more than 7.5 h, the molar ratio begins to stabilize, probably due to the equilibrium between *myo*-inositol and IPs in the present solvothermal environment.
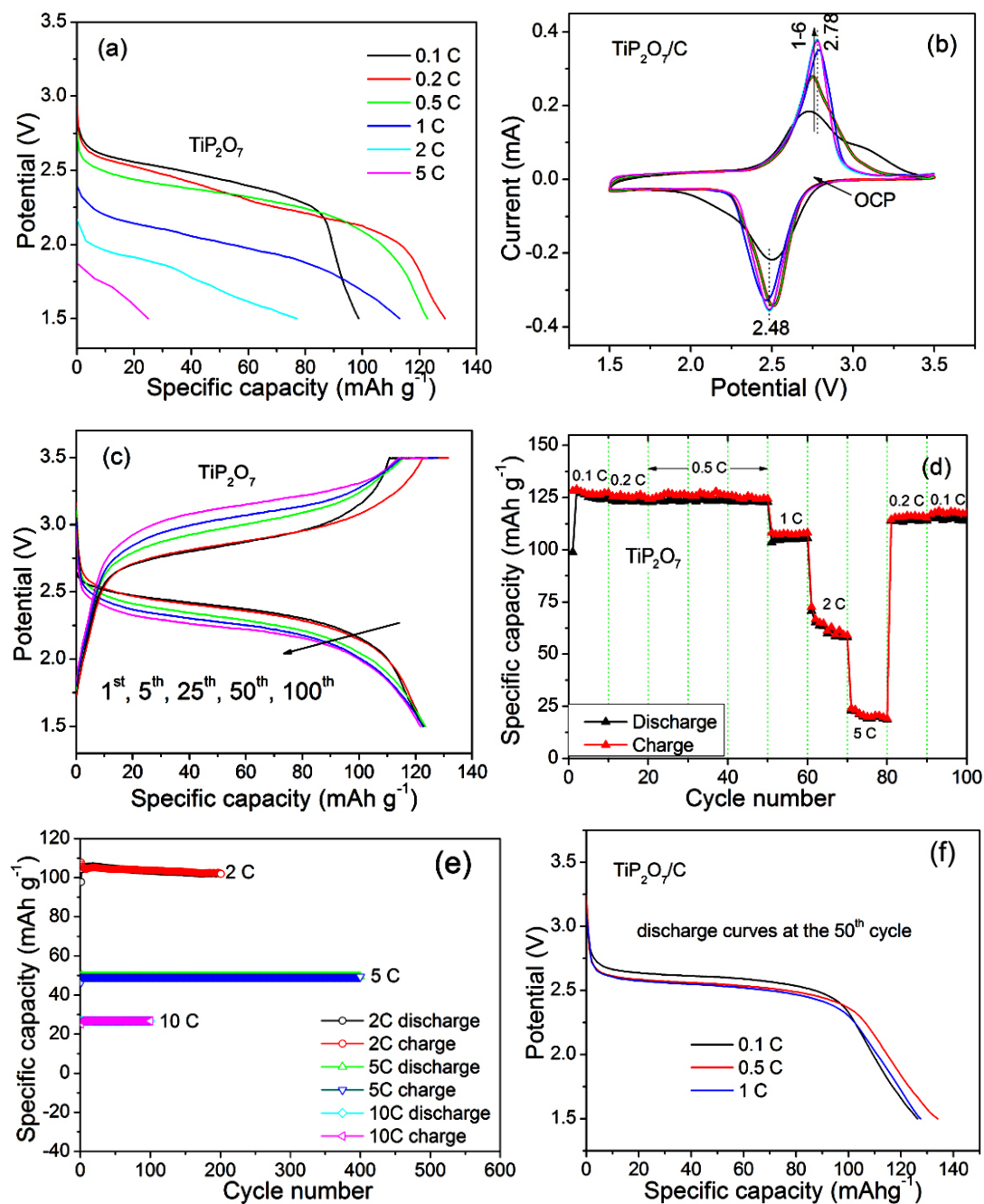
S10. Electrochemical performance of the samples

Fig. S10. (a) Initial discharge curves at different rates for TiP_2O_7; (b) cyclic voltammograms of TiP_2O_7/C cycled at 0.1 mv s^{-1}; (c) charge/discharge curves of TiP_2O_7 cycled at 0.5 C; (d) cycling performance at various rates for TiP_2O_7; (e) cycling performance of TiP_2O_7/C nano-aggregates; and (f) discharge curves of the 50th for TiP_2O_7/C operating at 0.1, 0.5, and 1 C.

S11. BET analysis of TiP$_2$O$_7$/C nanoparticle aggregates

Fig. S11. Sorption isotherms and pore size distribution of TiP$_2$O$_7$/C nano-aggregates.

Table S3. BET specific surface area and pore parameters of TiP$_2$O$_7$/C nano-aggregates.

Sample	S_{BET} (m^2 g^{-1})	Total pore volume (cm^3 g^{-1})	Total pore area (m^2 g^{-1})	Micropore volume (cm^3 g^{-1})	Micropore area (m^2 g^{-1})	Average pore width (nm)	S_{micro}/S_{BET} (%)
TiP$_2$O$_7$/C	30.6	0.08	25.0	0.0021	3.9	10.7	12.7

References (ESI)

1 S. T. Norberg, G. Svensson and J. Albertsson, *Acta Cryst.*, 2001, **C57**, 225–227.

2 J. Emsley, Chem. Soc. Rev., 1981, **9**, 91–124.

3 C. A. Poutasse, R. O. Day and R. R. Holmes, *J. Am. Chem. Soc.*, 1984, **106**, 3814–3820.

4 V. M. F. Hammer, E. Libowitzky and G. R. Rossman, *Am. Minera.*, 1998, **83**, 569–576.

5 L. Benco, D. Tunega, J. Hafner and H. Lischka, *J. Phys. Chem.* B, 2001, **105**, 10812–10817.

6 M. Pourayoubi and A. R. Mahjoub, *J. Iran. Chem. Soc.*, 2010, **7**, 864–874.

7 J. Lehrfeld, *J. Agric. Food Chem.*, 1994, **42**, 2726–2731.

8 S. Bruque, M. A. G. Aranda, E. R. Losilla, P. Olivera-Pastor and P. Maireles-Torres, *Inorg. Chem.*, 1995, **34**, 893–899.

9 C. Bretti, R. M. Cigala, G. Lando, D. Milea and S. Sammartano, *J. Agric. Food Chem.*, 2012, **60**, 8075–8082.

10 U. Ulusoy, S. Şimşek and Ö. Ceyhan, *Adsorption*, 2003, **9**, 165–175.

11 Z. Shi, Q. Wang, W. Ye, Y. Li and Y. Yang, *Micropor. Mesopor. Mater.*, 2006, **88**, 232–237.

12 C. Lai, W. Wang, J. Gao, Y. Wang, S. Ye, L. Li and C. Wang, *RSC Adv.*, 2013, **3**, 13137–13139.

13 V. Aravindan, M. V. Reddy, S. Madhavi, S. G. Mhaisalkar, G. V. Subba Rao and B. V. R. Chowdari, *J. Power Sources*, 2011, **196**, 8850–8854.

14 S. Patoux and C. Masquelier, *Chem. Mater.*, 2002, **14**, 5057–5068.

15 M. Satya Kishore, V. Pralong, V. Caignaert, U. V. Varadaraju and B. Raveau, *J. Power Sources*, 2007, **169**, 355–360.

16 Y. Hao, C. Wu, Y. Cui, K. Xu, Z. Yuan and Q. Zhuang, *Ionics*, 2014, DOI 10.1007/s11581-014-1065-8.